Chemistry Europe
European Chemical Societies Publishing

WILEY VCH

Excellence in Chemistry Research

Announcing our new flagship journal

- Gold Open Access
- Publishing charges waived
- Preprints welcome
- Edited by active scientists

Meet the Editors of *ChemistryEurope*

Luisa De Cola
Università degli Studi di Milano Statale, Italy

Ive Hermans
University of Wisconsin-Madison, USA

Ken Tanaka
Tokyo Institute of Technology, Japan

ChemCatChem

Research Article
doi.org/10.1002/cctc.202201336

Chemistry Europe
European Chemical Societies Publishing

www.chemcatchem.org

Special Collection

Electrocatalytic Oxidative Coupling of Methane on NiFe Exsolved Perovskite Anode: Effect of Water

Jaesung Kim,[a] Matthew Ferree,[a] Seval Gunduz,[a] Jean-Marc M. Millet,[b] Mimoun Aouine,[b] Anne C. Co,[c] and Umit S. Ozkan*[a]

Oxidative coupling of methane (OCM) can be performed electrocatalytically by utilizing solid oxide cells, which provide a readily controlled oxygen supply through dense electrolytes. $La_{0.7}Sr_{0.2}Ni_{0.2}Fe_{0.8}O_3$ (LSNF) perovskite is an effective anode for OCM. Its surface characteristics and electrocatalytic activity can be improved by reduction and the resultant exsolution of bimetallic NiFe nanoparticles from its bulk. X-ray diffraction (XRD) and environmental transmission electron microscopy proved that the evolution of hetero-phases under reducing environment resulted in bimetallic NiFe nanoparticles being formed on the surface. A 36% improvement in C_{2+} hydrocarbon production rate was achieved due to the reduction of LSNF with the exsolved NiFe nanoparticles. Co-feeding of H_2O enhanced selective conversion of CH_4 resulting in the production rate of C_{2+} hydrocarbons being increased by 56%. Analysis of impedance spectra and in-situ DRIFTS under a CH_4+H_2O atmosphere provided an understanding for the enhancement on the electrocatalytic OCM.

Introduction

Currently, methane is produced in large quantities due to recent advances in the shale gas refining technologies.[1] In conventional processes, steam reforming is typically required to convert methane into valuable chemicals such as alcohols and olefins. The steam reforming process is highly endothermic and inefficient and, as a result, makes it unprofitable, limiting methane utilization. A more efficient approach may be to eliminate the reforming step from the process and, instead, convert methane directly into valuable compounds.[2]

Direct conversion of methane can be achieved in a heterogeneous catalysis process either through non-oxidative or oxidative coupling. The change in Gibbs free energy for non-oxidative and oxidative couplings of methane calculated at temperatures ranging from 25 °C to 900 °C is shown in Figure 1 (thermodynamic parameters are provided in the supporting information) and it demonstrates the inherent challenges associated with methane conversion. The production of C_2H_6 and C_2H_4 through non-oxidative coupling of methane requires positive Gibbs free energy changes at all temperature ranges, indicating that these reactions are not thermodynamically favorable, while carbon formation is thermodynamically favorable at high temperatures (Figure 1(a)). Coke deposition on the

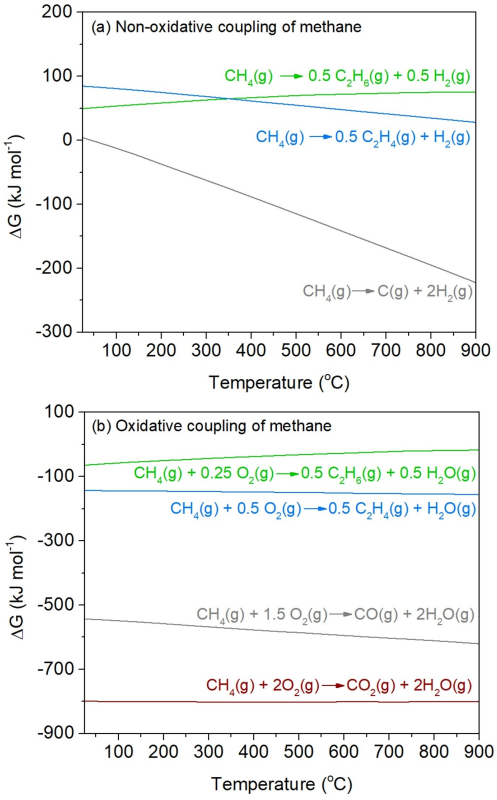

Figure 1. The changes in the Gibbs free energy for potential individual reactions involved in (a) non-oxidative coupling of methane and (b) oxidative coupling of methane at temperatures ranging from 25 °C to 900 °C.

[a] J. Kim, M. Ferree, S. Gunduz, Prof. U. S. Ozkan
William G. Lowrie Department of Chemical and Biomolecular Engineering
The Ohio State University
151 W. Woodruff Ave.
Columbus, OH 43210 (USA)
E-mail: Ozkan.1@osu.edu
[b] Prof. J.-M. M. Millet, Dr. M. Aouine
Institut de Recherche sur la Catalyse et l'Environnement de Lyon
UMR 5256 Université Claude-Bernard Lyon 1
69626, Villeurbanne Cedex (France)
[c] Prof. A. C. Co
Department of Chemistry and Biochemistry
The Ohio State University
100 W. 18th Ave.
Columbus, OH 43210 (USA)

Supporting information for this article is available on the WWW under https://doi.org/10.1002/cctc.202201336

Special Collection *This publication is part of a Special Collection on "French Conference on Catalysis 2022". Please check the ChemCatChem homepage for more articles in the collection.*

catalyst surface would lead to deactivation of the catalyst, which is an inherently challenging issue in the non-oxidative coupling of methane.[3] In contrast, the formation of C_2H_6 and C_2H_4 through oxidative coupling of methane (OCM) is thermodynamically favorable at all temperatures (Figure 1(b)). The difficult issue of the OCM, however, is that the oxidation of methane to CO and CO_2 is a more thermodynamically favorable reaction than the coupling of methane. A strategy for improving the selectivity of C_{2+} hydrocarbons, including ethane and ethylene, is to use a membrane reactor capable of operating OCM at low partial pressures of oxygen. Specially, solid oxide cells (SOCs) which consist of solid oxide electrolyte membranes and electrodes may effectively control the oxygen ion flow with an appropriate current.[2e,4] Oxygen supply control is important for OCM because the yields to C_{2+} hydrocarbons depend on a half order of O_2 partial pressure while deep oxidation of CH_4 to CO and CO_2 shows first-order dependence on the partial pressure of oxygen.[5] When applied to an electrocatalytic system, OCM has the advantage of being spontaneous, thus generating electricity.

Even with these advantages, however, selective conversion of methane from OCM is still challenging for SOCs because most catalysts having mixed ionic and electronic conductivity are chemically reactive for a deep oxidation of methane to CO and CO_2.[2a,4,6]

OCM has been shown in kinetic studies to yield up to a maximum of 28–30% C_{2+} hydrocarbons since the rate of hydrogen abstraction from C_{2+} products is greater than the rate of hydrogen abstraction from methane on the majority of catalysts.[7] In order to achieve higher yields for OCM, its kinetics and mechanism should be better understood. Literature has indicated that certain substances that result from the oxidation of methane may act as feedback control intermediates. As an example, water had a positive effect on OCM over Li/MgO catalyst, explained by the generation of additional active sites on the catalyst surface aided by adsorbed water.[8] A similar marked effect of water on the OCM reaction rate and selectivity over $NaWMn/SiO_2$ catalyst was reported as being caused by catalytic generation of $OH^{\bullet}$ radicals and their significant role in homogeneous activation of methane without net H_2O consumption.[9] Another study suggests that re-oxidation of oxygen vacancy sites is facilitated by water molecules, leading to an efficient turnover of the active sites.[10]

Perovskite materials based on Fe, such as $La(Sr)FeO_3$, exhibit a range of beneficial properties for use in electrocatalysis. They are chemically compatible with electrolyte materials, have high electrical conductivity, and are stable in both oxidizing and reducing atmospheres.[11] The electrocatalytic activity of these materials can be further enhanced by introducing A-site deficiency and B-site doping. Additionally, the formation of exsolved B-site metal nanoparticles on the surface of the perovskite material when it is exposed to a hydrogen atmosphere has been shown to significantly improve its electrochemical activity.[12]

In this study, we explored $La_{0.7}Sr_{0.2}Ni_{0.2}Fe_{0.8}O_3$ (LSNF) as an anode catalyst in a solid oxide cell working in ion pump mode for OCM. Reduction of LSNF perovskite treated under reducing environment at elevated temperatures exsolved bimetallic NiFe nanoparticles on the surface, which are active and selective species for OCM. The exsolution of bimetallic NiFe nanoparticles and the resultant improvement on the electrochemical performance of LSNF anode for OCM were verified by an analysis of surface and bulk characteristics of LSNF catalysts.

Results and discussion

Structural analysis of LSNF

Transmission electron microscopy (TEM) and X-ray diffraction (XRD) have been used to study the crystal structure of LSNF powders under air. In Figure 2(a), the LSNF powder calcined at 1000 °C shows a sharp peak and a clean base line in the XRD spectrum, which indicates perfect crystallinity. Based on the XRD pattern, the LSNF has a distorted orthorhombic crystal structure with a Pbnm space group, which is identical to $LaFeO_3$ perovskite oxide.[13] An additional confirmation of the perovskite structure has been obtained using Rietveld refinement. The lattice parameters calculated using the UnitCell program are a = 0.5523 nm, b = 0.4594 nm, and c = 0.7784 nm, resulting in the lattice volume being 0.23622 nm^3.[14] As a result of the Ni atom doping at the B site, the lattice unit cell volume of LSNF was smaller than the reference $LaFeO_3$, 0.24224 nm^3. This is due to the smaller ionic radius of Ni ion than Fe ion. The TEM image of the LSNF powder at room temperature are shown in Figure 2(b). Inverse Fast Fourier Transform (IFFT) was attempted

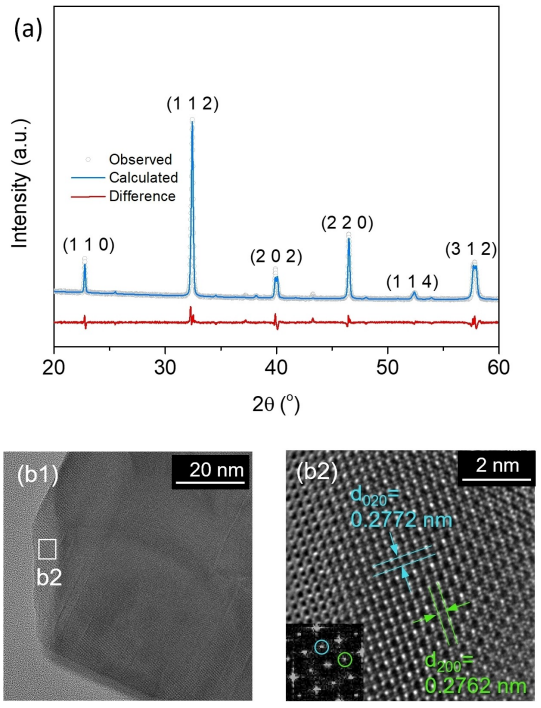

Figure 2. (a) Room temperature XRD pattern of LSNF and Rietveld refinement, (b1) TEM image of LSNF at room temperature, (b2) enlarged TEM image from (b1) with lattice fringes and inverse fast Fourier transform (IFFT).

on the region in Figure 2(b2). The obtained lattice fringes for LSNF are 0.2772 nm and 0.2762 nm, corresponding to a (020) and (200) planes of $LaFeO_3$ at 90°, respectively. Indexing parameters are provided in Table S2.

Exsolution of NiFe nanoparticles

Exsolution of NiFe nanoparticles as well as structural characteristics of LSNF perovskite in a reducing environment have been investigated by temperature-programmed reduction (TPR), XRD, Raman spectroscopy and environmental transmission electron microscopy (ETEM). In the TPR experiment conducted under 30 ccm of 5% H_2/N_2, the H_2O signal (m/z = 18) was monitored as a function of temperature up to 1000 °C as shown in Figure 3(a). The LSNF showed an initial peak at about 440 °C in the TPR profile, which can be explained by the reduction of nickel. Upon reaching temperatures greater than 650 °C, both iron and nickel are reduced, resulting in water.[15]

The XRD pattern of the LSNF reduced at 800 °C under 5% H_2/N_2 for 5 h (Red-LSNF) reveals the hetero-phases emerging, including NiFe alloy, Ruddlesden-Popper (RP) phase La_2NiO_4, and La_2O_3 (Figure 3(b)). The weight fraction of the transformed NiFe alloy and La_2NiO_4 phase was calculated being 6.5% and 32.8%, respectively, by Rietveld refinement. It is typical that La_2O_3 is formed in conjunction with exsolution.[16] The structural transformation to RP phase, La_2NiO_4, was also confirmed by Raman spectra shown in Figure 3(c). The internal vibration of FeO_6 octahedra in perovskite could be responsible for the bands at 296, 434, 480 and 562 cm^{-1}.[17] The band at 144 cm^{-1} may arise due to the motion of lanthanum or strontium ion inside the crystal lattice. The two Raman modes on La_2NiO_4 observed at 434 cm^{-1} and 216 cm^{-1} can be assigned to the Ni–O(2) stretching (A_{1g}) and apical oxygen vibration along the a- and b-axes with E_g symmetry, respectively.[18] The Red-LSNF exhibited contributions from both of the phases. RP phase with a general formula, $A_{m+1}B_mO_{3m+1}$ ($m > 1$), has a higher oxygen stoichiometry than a normal perovskite, providing a better mixed electronic and ionic conductivity.[19]

The exsolution of nanoparticles from LSNF induced by the reduction were observed by ETEM at 700 °C under 1 mbar of H_2 environment in Figure 4(a). The results of Inverse fast Fourier transform (IFFT) on the nanoparticle show that the lattice fringes of 0.2111 nm and 0.2050 nm at 90° correspond to (111) and (11-1) planes of $Fe_{0.570}Ni_{0.493}$ alloy (Table S3). It was quantitatively determined that the NiFe alloy nanoparticle has near 1 to 1 atomic composition of Ni and Fe using scanning transmission electron microscope (STEM) with energy dispersive spectroscopy (EDS) in Figure S1. The exsolution of the B-site atoms from the perovskite oxide is dependent on the formation of partial Schottky defects in the perovskite lattice as follows (Eq. 1):[20]

$$B_B^X + \frac{m}{2}O_O^X \leftrightarrow V_B^{m'} + \frac{m}{2}V_O^{\bullet\bullet} + B_{surface} + \frac{m}{4}O_2(g) \quad (1)$$

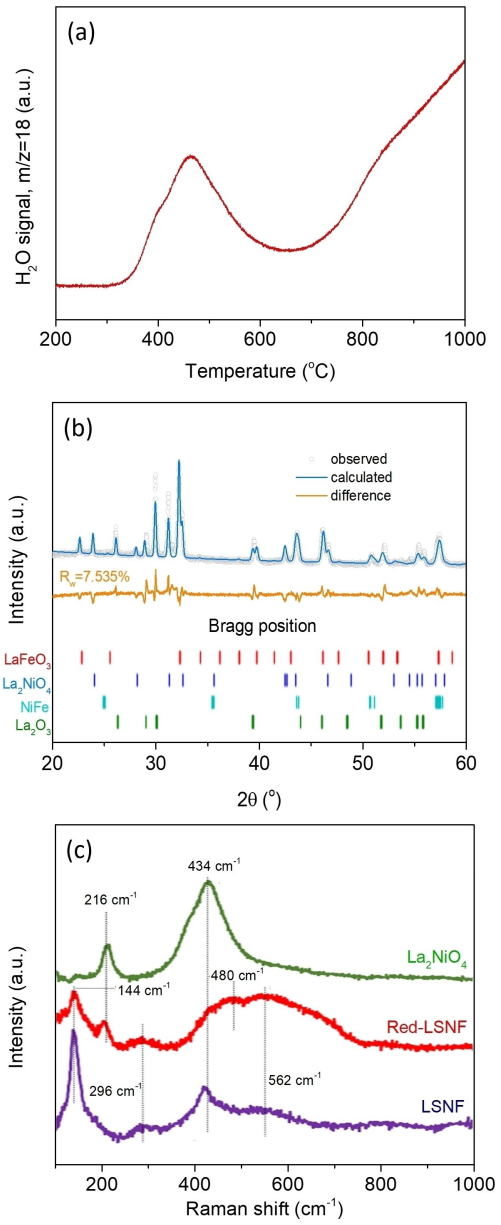

Figure 3. (a) Temperature-programmed reduction profile of LSNF, (b) XRD pattern of Red-LSNF with Rietveld refinement analysis, (c) Raman spectra of LSNF, Red-LSNF, and La_2NiO_4.

Here, B_B^X and O_O^X are B-site atoms (Ni or Fe) and oxygen ions in the perovskite lattice, respectively, and $B_{surface}$ is a neutral B atom segregated at the surface. $V_B^{m'}$ and $V_O^{\bullet\bullet}$ are the B-site and oxygen vacancies, respectively. The main driving force for the process is the Gibbs free energy change from B^{n+} to B^0.[21] Additionally, A-site deficiency in perovskite could be a general driving force for B-site exsolution because exsolution results in stable defect-free ABO_3 stoichiometry.[22]

Figure 4(b) shows the Red-LSNF surface morphology, with particle number density as a function of particle size. The parent LSNF surface was uniformly coated with NiFe nanoparticles, an important characteristic of exsolution over physical deposition. NiFe nanoparticles in this study were observed within a similar

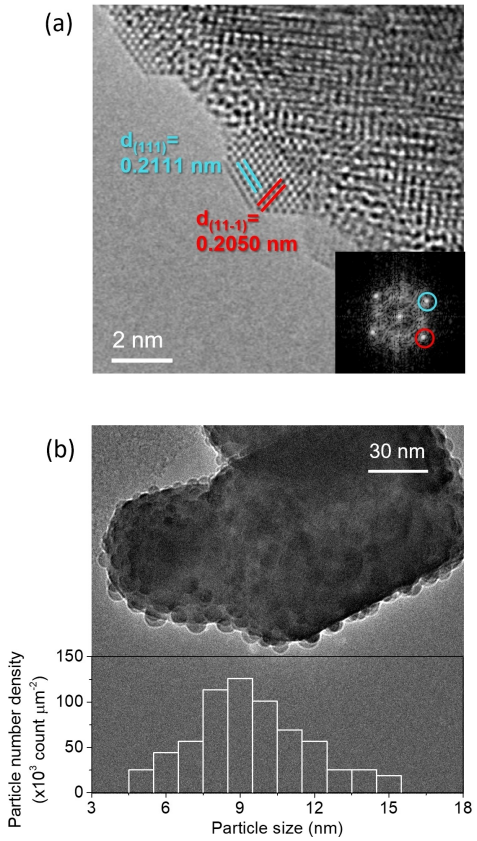

Figure 4. (a) In-situ TEM image under 1 mbar of H_2 atmosphere at 700 °C with lattice fringes and IFFT, (b) in-situ TEM image of Red-LSNF under 1 mbar of H_2 atmosphere at 800 °C with particle number density.

size range as those observed with strontium titanate doped perovskites, and much smaller than those observed with Ni doped $Sr_2Fe_{1.5}Mo_{0.5}O_6$ double perovskites.[23]

Another advantage of exsolution is stability of the exsolved nanoparticles at high temperatures.[24] In the real time captured images in Figure 5 and video in Appendix Video 1, the NiFe nanoparticles shows a dynamic lateral movement in a time range from 1.35 s to 1.93 s, but they are well anchored to the perovskite. As a result of such a firm attachment to the parent perovskite, exsolution effectively prevents nanoparticles from sintering at high temperatures. Figure S2 shows the socket anchoring the exsolved particle. It is also noted that the perovskite changes its crystal structure from orthorhombic to tetragonal where the exsolution takes place.

Investigation of elemental oxidation state

Electrocatalytic performance of LSNF electrodes is significantly affected by the oxidation state and atomic concentration of its elements on their surfaces. The LSNF and Red-LSNF were investigated using X-ray photoelectron spectroscopy (XPS). The XPS spectra in the Fe 2p, O 1s and Sr 3d regions for both LSNF and Red-LSNF were plotted as a function of binding energy in Figure 6. Also presented is the atomic composition calculated from the XPS spectra of the samples.

An analysis of the binding energies of the Fe $2p_{3/2}$ peak and the satellite peak was proposed to determine the presence of Fe^{2+} and Fe^{3+} by Gautier-Soyer and co-workers.[25] Compounds of the Fe^{3+} ion possess approximately 8 eV of difference between the Fe $2p_{3/2}$ peak and the satellite peak, while compounds of the Fe^{2+} ion possess 4.3–5.65 eV of difference. As the difference was estimated to be around 8 eV for both LSNF and Red-LSNF in Figure 6(a,d), the data suggest Fe^{3+} species being prevalent on the surface even after the reduction. In the deconvoluted XPS spectra in Figure 6(a), the peaks located at the binding energy of 709.5 eV and 711.4 eV can be assigned to Fe^{3+} $2p_{3/2}$ and Fe^{4+} $2p_{3/2}$, respectively for LSNF.[26] Those peaks were shifted to 710.0 eV and 712.12 eV, respectively, after the reduction (Figure 6(d)). The decrease in Fe^{4+} species concentration from 49.7% to 43.8% and the advent of zerovalent Fe of 1.6% following the reduction of LSNF indicate a change in the oxidation state, although Fe^{3+} and Fe^{4+} species still remain dominant. The Fe^{3+}/Fe^{4+} redox pairs in lanthanum ferrite perovskites are of great significance in the electronic conductivity of the materials because these pairs act as p-type charge carriers.[27]

Figure 6(b,e) shows the O 1s XPS spectra of LSNF and Red-LSNF. The peaks in O 1s XPS spectra were deconvoluted into two peaks for lattice oxygen at 528.4 eV and for surface oxygen at 531.3 eV, respectively.[28] The surface oxygen may include hydroxyl group and carbonate species. During the reduction under hydrogen atmosphere, a hydroxyl group is formed on the surface of Red-LSNF, which could account for the higher concentration of surface oxygen. In addition, the oxygen vacancies on the surface caused by reduction can be occupied by atmospheric CO_2 resulting in the formation of carbonate.

Sr 3d on LSNF and Red-LSNF appears to consist of two distinct species both of which have an oxidation state of +2 in Figure 6(c,f). The strontium oxide species detected on LSNF corresponded to the Sr 3d 5/2 peak at 131.7 eV, whereas the strontium carbonate species was detected at 133.2 eV.[29] The atomic concentration of carbonate on the surface of Red-LSNF was 64.9%, which is significantly higher than 36.4% carbonate on LSNF. The reason is that the reduction of LSNF significantly increased the concentration of oxygen vacancies on the surface, which have been proposed to be the adsorption site for CO_2.[30] Also, strontium oxide species have been reported to cover the surface of perovskites as a result of their migration abilities, and tend to react with CO or CO_2 in the atmosphere, resulting in stable strontium carbonate species.[31]

Analysis of surface basicity

The formation of heterogeneous phases La_2NiO_4 and zerovalent NiFe on the surface of Red-LSNF might affect its surface adsorption-desorption characteristics. In addition, the oxygen vacancies created during the reduction could serve as an effective adsorption site for CO_2. Using CO_2 as the probe molecule, TPD-DRIFTS were conducted on both samples to

Research Article
doi.org/10.1002/cctc.202201336

Chemistry Europe
European Chemical Societies Publishing

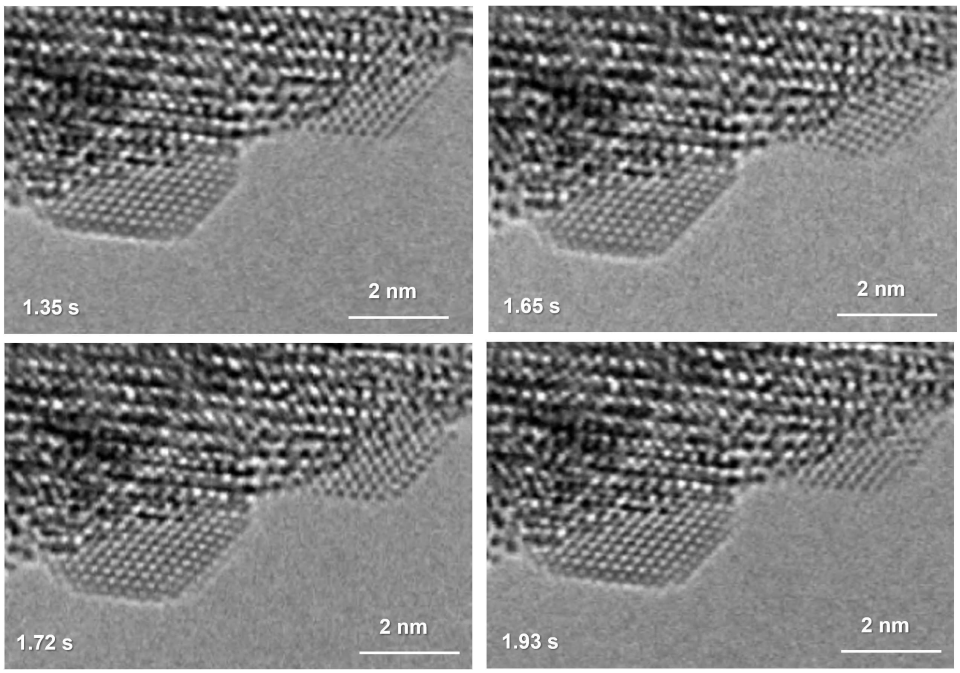

Figure 5. Lateral shape dynamics of exsolved nanoparticles under 1 mbar of H_2 atmosphere at 700 °C. In-situ TEM images captured from Appendix Video 1 at different times from 1.35 s to 1.93 s.

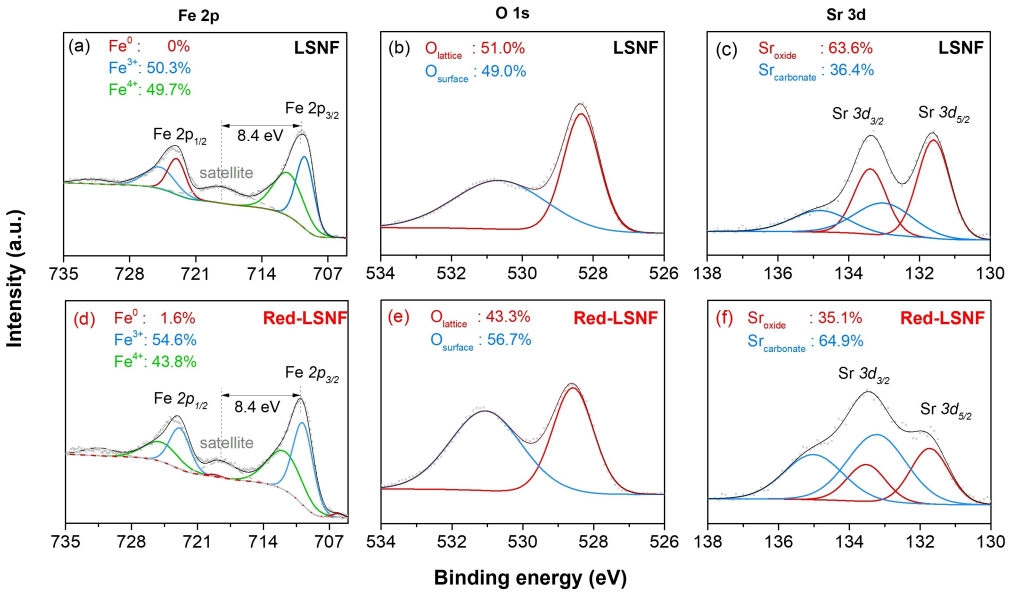

Figure 6. X-ray photoelectron spectra of LSNF and Red-LSNF: (a,d) Fe 2p, (b,e) O 1s, (c,f) Sr 3d.

examine the differences between LSNF and Red-LSNF with respect to adsorption-desorption characteristics (Figure 7). The adsorption peaks for CO_2 on both samples, 2360 cm^{-1} and 2330 cm^{-1}, are evidence that the CO_2 molecules were molecularly adsorbed. The carbonate chemisorbed species, however, were only found on Red-LSNF.[27,32] There were molecular CO_2 peaks present on LSNF up to 200 °C, which disappeared completely at 250 °C, but those peaks remained visible on Red-LSNF until 250 °C, indicating a stronger adsorption of CO_2. Contrary to this, chemisorbed CO_2 peaks were only observed on Red-LSNF at 1530 cm^{-1} and 1380 cm^{-1}, corresponding to bidentate and monodentate species, respectively. An explanation for this observation can be found in the increased concentration of oxygen vacancy sites on the Red-LSNF surface, which act as adsorption sites.[30] It has been reported that Ni nanoparticles exhibit strong interactions with CO_2, especially when combined with oxygen vacancies.[33] It is also likely that

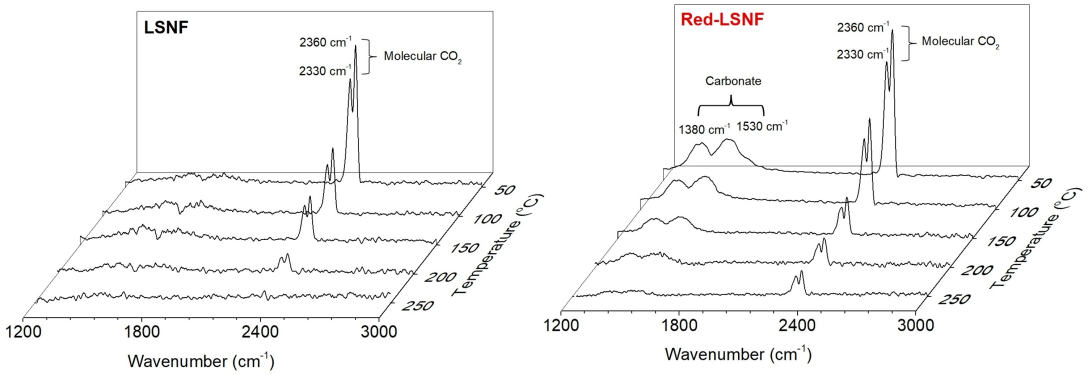

Figure 7. In-situ TPD-DRIFTS of CO_2 on LSNF and Red-LSNF.

$SrCO_3$ is responsible for the chemisorbed CO_2 peaks in the DRIFTS spectra on Red-LSNF.[34]

Electrocatalytic OCM

An evaluation of the electrocatalytic activity of the LSNF cell for oxidative methane coupling (OCM) performed using 10 ccm of CH_4 at 800 °C. The LSNF cell was reduced under 5% H_2/N_2 at 800 °C for 5 h to prepare the Red-LSNF prior to the operation of electrocatalytic OCM. OCM results for LSNF and Red-LSNF anodes at 800 °C are presented in Table 1. The selectivity towards C_{2+} hydrocarbons including C_2H_4, C_2H_6, and C_3H_6 increased from 37.1% to 41.5% due to the reduction of LSNF, resulting in 35.5% improvement in the production rate. In addition, the reduction of LSNF promoted the dehydrogenation of C_2H_6 to C_2H_4 as indicated by the increase in the ratio of alkene to alkane ratio. The improvement on the selective conversion of CH_4 can be attributed to the NiFe nanoparticles exsolved on the surface of LSNF and the increased surface basicity induced by the reduction.

The electrocatalytic OCM on the Red-LSNF anode produced more C_{2+} hydrocarbons as the current density increased (Figure 8 and Table 2). The production rate of C_{2+} hydrocarbons was measured as 31 μmol cm^{-2} h^{-1} at open-circuit voltage (OCV), which increased with the increase in the applied current. This means that OCM is an electrocatalytically activated process, with oxidative coupling of CH_4 being favored over non-oxidative coupling. When 150 mA cm^{-2} of current density was applied, the production rate of C_{2+} hydrocarbons was 345 μmol cm^{-2} h^{-1}, which is 11 times higher than that under OCV. The highest selectivity of C_{2+} hydrocarbons were achieved 53.8% at 25 mA cm^{-2}. A similar button cell in a recent study achieved a C_{2+} hydrocarbons selectivity of around 30% and a production rate two orders of magnitude lower than this study.[2e] While there have been other studies on electrocatalytic OCM, their results are not directly comparable to the results of this study due to differences in the reactor setup, applied

Table 1. OCM results on LSNF and Red-LSNF anode under 150 mA cm^{-2} at 800 °C.

Anode	Carbon selectivity [%]					C_{2+} hydrocarbons Selectivity [%]	Conversion [%]	C_{2+} hydrocarbons Production rate[a] [μmol cm^{-2} h^{-1}]	Alkene[b] /Alkane	Carbon balance [%]
	C_2H_4	C_2H_6	C_3H_6	CO	CO_2					
LSNF	19.1	16.2	1.9	1.5	61.3	37.1	7.6	255	1.3	92.1
Red-LSNF	21.4	15.5	4.6	3.3	55.2	41.5	9.7	345	1.7	94.5

[a] C_{2+} hydrocarbons include C_2H_4, C_2H_6, and C_3H_6, [b] Alkene includes C_2H_4 and C_3H_6.

Table 2. Electrocatalytic OCM results on the Red-LSNF anode.

Current density [mA cm^{-2}]	Carbon selectivity [%]					C_{2+} hydrocarbons Selectivity [%]	Conversion [%]	Alkene /Alkane	C_{2+} Production rate [μmol cm^{-2} h^{-1}]	Faradaic efficiency [%]	Carbon balance [%]
	C_2H_4	C_2H_6	C_3H_6	CO	CO_2						
OCV	21.1	38.8	3.5	16.1	20.5	63.4	0.6	0.6	31	–	99.7
25	21.4	26.9	3.9	0.0	47.4	52.6	6.0	0.9	136	99.5	98.6
50	24.3	24.7	4.9	1.2	45.0	53.8	6.8	1.2	204	92.3	98.6
75	23.8	21.2	4.9	1.8	48.4	49.9	7.5	1.4	247	88.3	97.2
100	22.9	18.8	4.9	2.3	51.2	46.6	8.3	1.5	282	94.9	98.9
125	21.9	16.8	4.6	2.8	53.9	43.3	9.3	1.6	312	92.6	97.6
150	21.4	15.5	4.6	3.3	55.2	41.5	9.7	1.7	345	94.5	98.4

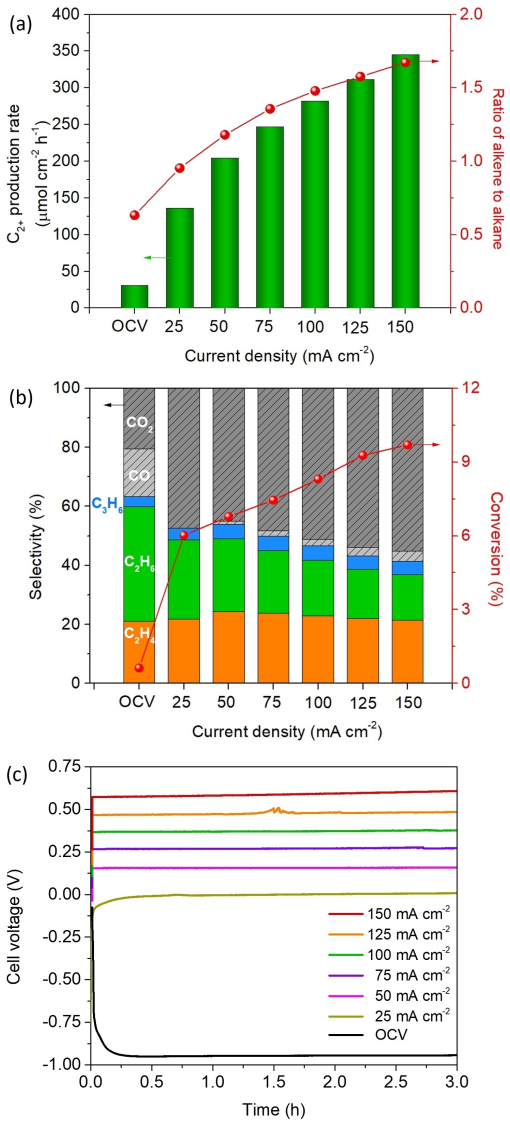

Figure 8. Electrocatalytic OCM results on the Red-LSNF cell at 800 °C at various current densities. (a) production rate of C_{2+} hydrocarbon and the ratio of alkene to alkane, (b) carbon selectivities and conversion, (c) time-on stream of the cell voltage.

voltage, and cycled product stream.[2a,4] Figure 8(a) shows that the alkene/alkane ratio increases as the applied current increases, which indicates that the electrochemical dehydrogenation of C_2H_6 is also facilitated by the oxygen supply, resulting in an alkene-to-alkane ratio of 1.7 at 150 mA cm^{-2}. The cell voltage was monitored for 3 h at each current density to determine the stability of the Red-LSNF anode for the electrocatalytic OCM (Figure 8(c)). In order to evaluate the stability of the Red-LSNF cell for the electrocatalytic OCM, a cell voltage was measured for 3 h at each current density, and it displayed great thermochemical stability during that period of time (Figure 8(c)). The stability can be attributed to the anchoring effect of the exsolved NiFe nanoparticles.

The electrochemical impedance spectra of the Red-LSNF cell were obtained under OCV and at different current densities for the OCM as seen in Figure 9(a). The x-axis intercept in the Nyquist plots at high frequency were shifted to zero by subtracting the ohmic resistance (Z_b). There was a significant difference between the polarization resistance at different current densities under OCV and those when current is applied. This means that OCM reaction is electrocatalytically activated and the polarization resistance considerably decreased by the supplied oxygen ions. Due to overlapping arcs, it was difficult to select an equivalent circuit based on an assumption about

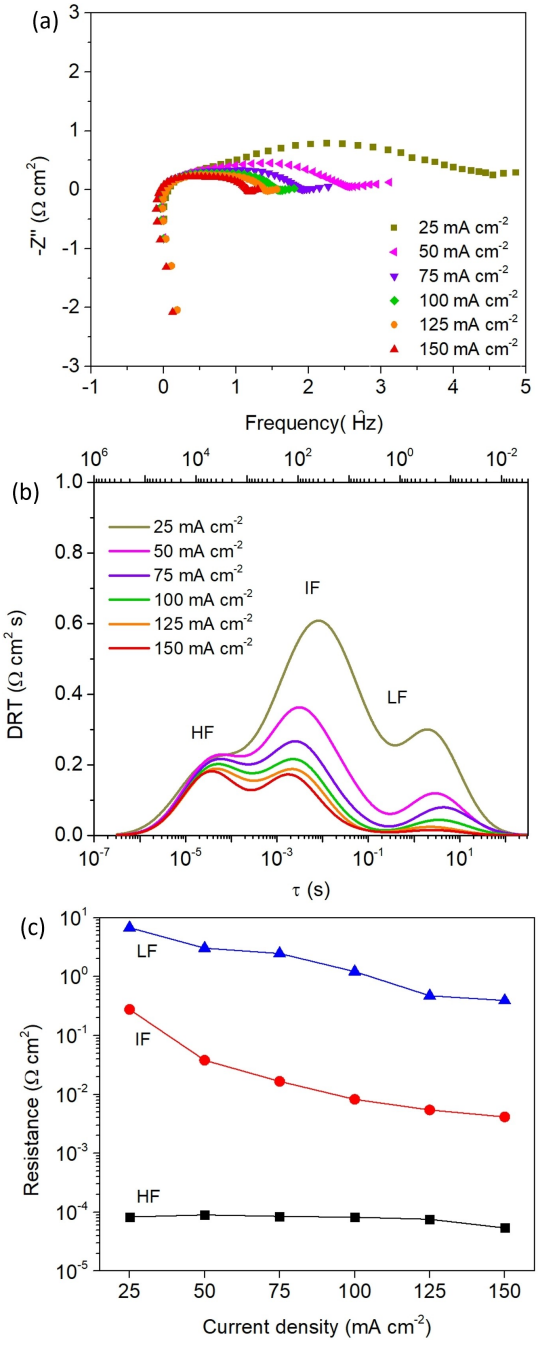

Figure 9. (a) Electrochemical impedance spectra, (b) distribution of relaxation time, and (c) polarization resistance for electrocatalytic OCM at 800 °C at different current densities.

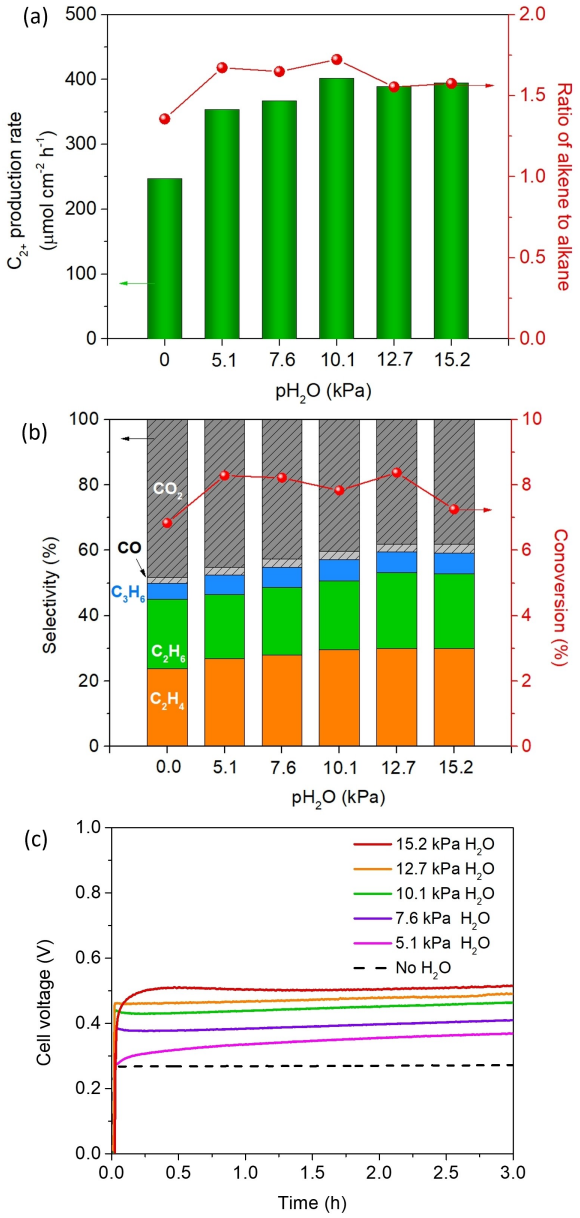

Figure 10. Electrocatalytic OCM results on the Red-LSNF cell at 800 °C at 75 mA cm^{-2} with co-feeding of H_2O. (a) production rate of C_{2+} hydrocarbon and the ratio of alkene to alkane, (b) carbon selectivities and conversion, (c) time-on stream of the cell voltage.

the impedance spectra. The distribution of relaxation time (DRT) was investigated in order to identify key sub-steps involved in the electrode reaction process. DRT is useful for directly deriving characteristic distribution patterns from impedance spectra without assuming a model of an equivalent circuit. Calculation for DRT is based on solving a Fredholm integral equation, assuming the impedance is $Z^*(\omega) = Z'(\omega) - jZ''(\omega)$, where $Z^*(\omega)$ is the complex impedance and Z' and Z'' are the real and imaginary parts of complex impedance, respectively (Eq. 2).

$$Z^* = R_\infty + R_p \int_{-\infty}^{+\infty} \frac{G(\log(\tau))}{1 + j\omega\tau} d(\log(\tau)) \quad (2)$$

where R_∞ is the series resistance, R_p is the total polarization resistance, G is the DRT and $\tau = RC$ is the relaxation time, R is the effective resistance and C is the effective capacitance, and ω is the angular frequency. When $\omega = 0$, $\int_{-\infty}^{+\infty} G(\log(\tau))d(\log(\tau)) = 1$. The equation can be deconvoluted to real and imaginary parts of the impedance as follows (Eqs. 3–4):

$$Z'(\omega) = R_\infty + \int_{-\infty}^{+\infty} \frac{F(\tau)}{1 + \omega^2\tau^2} d(\log(\tau)) \quad (3)$$

$$Z''(\omega) = R_p \int_{-\infty}^{+\infty} \frac{F(\tau)\omega\tau}{1 + \omega^2\tau^2} d(\log(\tau)) \quad (4)$$

where $F(\tau) = R_P G(\log(\tau))$ is the DRT. Combined real and imaginary parts of the impedance were used to calculate G in *(eq. 2)*. This ill-posed problem can be solved by various special mathematical algorithms. In order to solve the equation, DRTtools was used with a second order of regularization derivative and 0.001 of regularization parameter based on Tikhonov regularization.[35] The DRT results at different current densities are shown in Figure 9(b) and the calculated magnitude, phase, Z', and Z'' as a function of frequency for the calculation of DRT are provided with experimental values in Figure S3. Three characteristic peaks indexed as HF (high frequency), IF (intermediate frequency), and LF (low frequency) were observed in the response time (τ) range from 300 s to 10^{-6} s in the DRT spectra. The peak intensities of DRT all decreased with increasing applied current density in Figure 9(b). High frequency response time remained unchanged, while intermediate frequency response time decreased and low frequency response time increased. Since the integrated area represents the polarization resistance, the decrease in response time in DRT also indicates a decrease in polarization resistance. The integrated polarization resistance is shown in Figure 9(c) and Figure S4 shows the deconvoluted peaks. In the short response time range in 10^{-6} s and 2.7×10^{-4} s, the HF peak attributed to charge transfer showed a slight decrease, reaching approximately 0.20 Ω cm^2. The polarization resistance in HF region is normally constant since it is dependent on electrolyte, contact resistance at the interfaces, and current collectors.[36] The observed decrease in the resistance on the Red-LSNF electrode with the increase in applied current can be explained by the number of redox pair of Fe^{3+}/Fe^{+4} since lanthanum ferrite type perovskites follows a small polaron conduction mechanism.[27] The redox concentration of Fe^{3+}/Fe^{4+} pairs in the Red-LSNF would stay low under the reducing environment for OCM. When the current is applied, the oxygen supply could increase the number of the redox pair resulting in the electronic conductivity increasing. It has been reported that perovskite materials such as $(La_{0.75}Sr_{0.25})_{0.95}Cr_{0.5}Mn_{0.5}O_3$ show higher conductivity under oxidizing environment than under reducing environment.[37] R_{IF} in the response time range of 2.7×10^{-4} s to

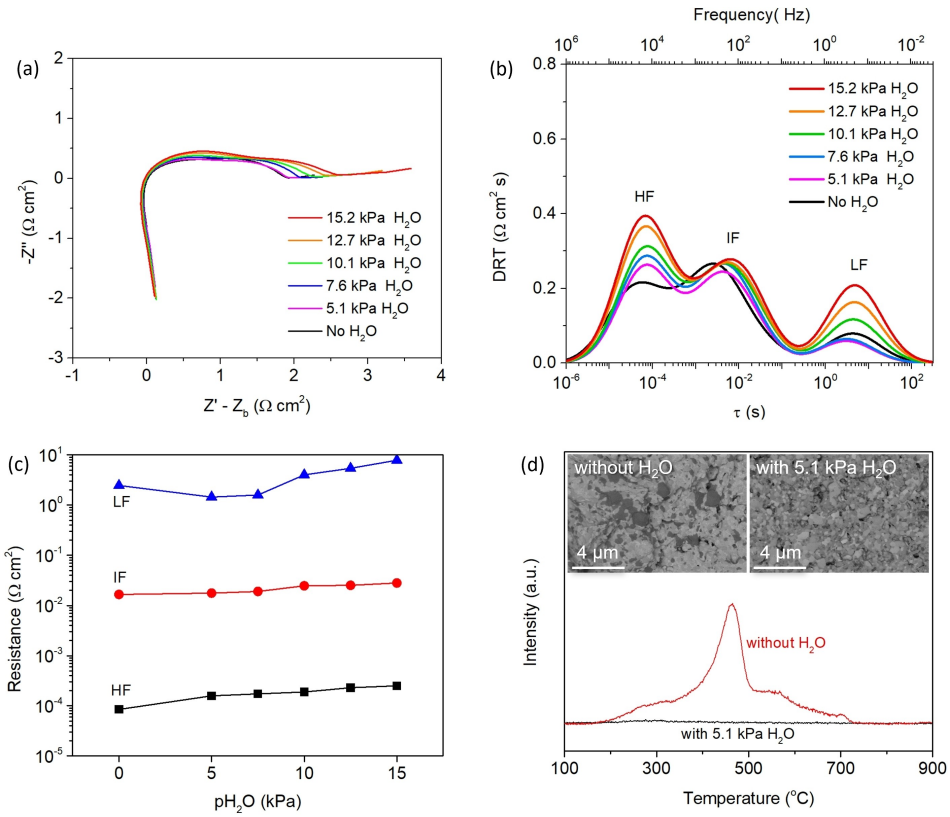

Figure 11. (a) Electrochemical impedance spectra, (b) distribution of relaxation time, and (c) polarization resistance for electrocatalytic OCM at 800 °C at 75 mA cm^{-2} with co-feeding of H_2O, (d) TPO profiles and SEM backscattered electron images on the post-OCM LSNF anodes without H_2O and with co-feeding of 5.1 kPa H_2O.

6.0×10^{-2} s associated with surface exchange and ion diffusion significantly decreased from 0.27 Ω cm^2 to 4.14×10^{-3} Ω cm^2 when the current density increased from 25 mA cm^{-2} to 150 mA cm^{-2}. The results indicate that the applied current enhances the surface reaction on the surface of the Red-LSNF anode, as oxygen ions present on the surface are able to react with methane. The polarization resistance at low frequency (R_{LF}) is attributed to mass transfer at the interface between the electrode and gas phase. The R_{LF} peak at 25 mA cm^{-2} was estimated to be 6.75 Ω cm^2, but it decreased to 0.39 Ω cm^2 at 150 mA cm^{-2}, indicative of the facilitated mass transfer. This is likely due to the enhanced surface reaction of CH_4 resulting in the concentration of CH_4 being decreased at the interface of the anode, leading to a greater concentration gradient.

The effect of H_2O on the electrocatalytic OCM

The effect of water on the electrocatalytic OCM was also examined at the applied current density of 75 mA cm^{-2}. Figure 10(a) and Table 3 show the production rate of C_{2+} hydrocarbons and the ratio of alkene to alkane at different partial pressures of H_2O in the range of 5.1 kPa to 15.2 kPa. A 56% increase in the production rate of C_{2+} hydrocarbons were observed when 10.1 kPa of H_2O was co-fed at 75 mA cm^{-2} compared to that without H_2O. Due to similar increases in the selectivity of C_2H_4 and C_2H_6, the ratio of alkene to alkane remained approximately the same. It is notable in Figure 10(b) that adding H_2O suppresses the deep oxidation of CH_4 to CO_2 by ~9% at 15.2 kPa resulting in the more selective conversion

Table 3. Electrocatalytic OCM results on the Red-LSNF anode with co-feeding of H_2O.

pH_2O [kPa]	Carbon selectivity [%]					C_{2+} hydrocarbons Selectivity [%]	Conversion [%]	Alkene /Alkane	C_{2+} Production rate [μmol cm^{-2} h^{-1}]	Faradaic efficiency [%]	Carbon balance [%]
	C_2H_4	C_2H_6	C_3H_6	CO	CO_2						
0	23.8	21.2	4.9	1.8	48.4	49.9	6.8	1.4	247	80.9	94.6
5.1	26.9	19.7	6.0	2.4	45.1	52.5	8.3	1.7	354	99.9	93.7
7.6	27.9	20.7	6.1	2.6	42.7	54.8	8.2	1.7	367	99.5	93.8
10.1	29.7	21.0	6.5	2.6	40.4	57.1	7.8	1.7	401	99.1	94.3
12.7	30.0	23.3	6.2	2.5	38.0	59.5	8.4	1.6	389	90.5	93.6
15.2	29.9	23.0	6.2	2.7	38.2	59.1	7.3	1.6	395	88.6	94.8

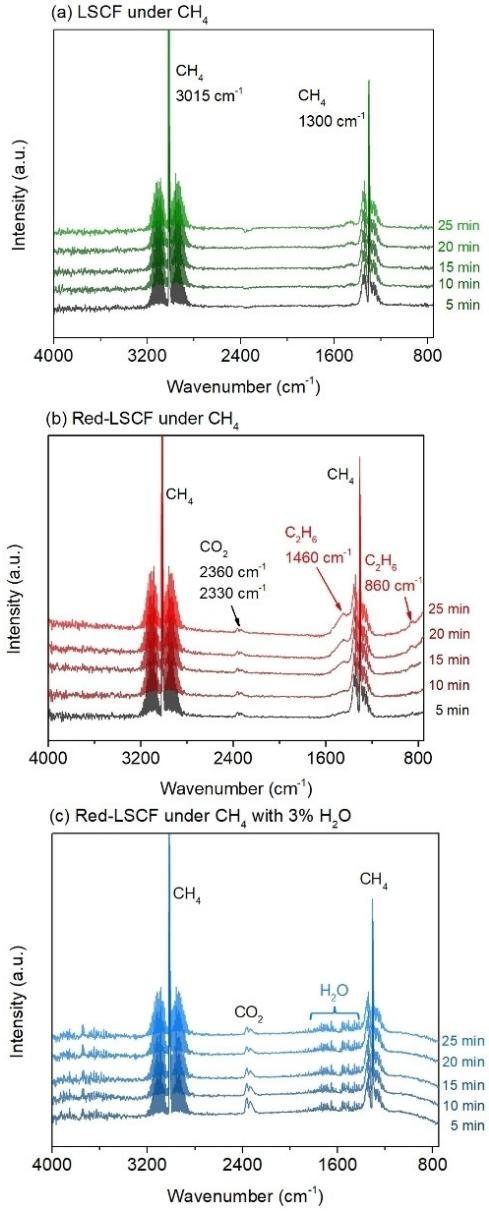

Figure 12. In-situ DRIFTS at 450 °C under CH_4 on (a) LSNF without H_2O, (b) Red-LSNF without H_2O, and (c) Red-LSNF with H_2O.

of CH_4 toward C_{2+} hydrocarbons. The positive effect of H_2O on OCM was prominent at less than 10.1 kPa of pH_2O. A similar result has also been reported in literature, that the addition of more than 8 vol% of H_2O doesn't further enhance the rate of methane oxidation over $NaWMn/SiO_2$.[10] This result implies that H_2O does not directly participate in methane oxidation reaction as a reactant. The fact that CO_2 selectivity was reduced, and CO selectivity stayed unchanged with co-feeding of H_2O also indicates that H_2O is not an active reactant for water-gas shift reaction and steam reforming of CH_4. It can be assumed that H_2O facilitates the re-oxidation of the surface oxygen vacancy sites resulting in the rapid turnover of the active sites.[10] In this assumption, the surface coverage with hydroxyl groups increases rapidly to a saturation level at low concentrations of H_2O. Hence, the increase of H_2O concentration above a certain point has no effect on the electrocatalytic OCM.

The co-feeding of H_2O also affected the cell voltage as shown in Figure 10(c). The cell voltage increased to 0.5 V when 15.2 kPa of H_2O was co-fed from 0.27 V without H_2O at 75 mA cm^{-2} of current density. The cell showed the thermochemical stability under the condition containing CH_4 and H_2O for 3 h. The impedance spectra for OCM under the condition is shown in Figure 11 with the corresponding DRT. The increase in the polarization resistance on the Red-LSNF cell was observed with the increase of H_2O concentration. The change in the polarization resistance at different H_2O concentration can be seen in detail with the DRT spectra in Figure 11(b) and the calculated magnitude, phase, Z', and Z'' are provided with experimental values in Figure S5. The DRT peaks in HF, IF, and LF region shifted to longer response and the peak intensities in HF and LF region noticeably increased with the increase of H_2O concentration, indicating the increase of polarization resistance of the cell.

The deconvoluted DRT spectra is shown in Figure S6 and the integrated peak area is plotted as polarization resistance in Figure 11(c). The increase of R_{HF} was observed with the increase of H_2O concentration. Essentially, H_2O affects the electrolyte/electrode contact interface or current collector of the cell, which may hinder the charge transfer. At intermediate frequency, the R_{IF} was almost constant at different current densities despite of the slight increase of the response time. In this regard, it appears that H_2O plays no direct role in the OCM reaction. When H_2O concentrations were lower at 5.1 kPa and 7.6 kPa, R_{LF} associated with mass transfer decreased, while when the concentrations were further increased, R_{LF} increased. The decrease of the R_{LF} at lower concentration of H_2O can be explained by the removal of coke deposited on the surface of the Red-LSNF anode since coke deposited on the active sites on the Red-LSNF must have a detrimental impact on the catalytic performance of the cell. Figure 11(d) compares temperature-programed oxidation (TPO) profiles and SEM backscattered images of the LSNF cells that has undergone OCM, with and without the co-feeding of 5.1 kPa H_2O. The post-OCM LSNF cell exhibits a significant CO_2 signal in the absence of H_2O co-feeding, but the signal is negligible when 5.1 kPa H_2O was co-fed. The darker regions of the SEM backscattered electron images correspond to lighter elements, such as carbon, while La, Sr, Fe, and Ni in the perovskite structure of the LSNF anode appear as lighter regions in the images. Several micrometer size carbon particles were deposited on the post-OCM LSNF anode surface that was not co-fed wit H_2O. On the other hand, bulky carbon is not visible on the post-OCM LSNF surface that was co-fed with 5.1 kPa H_2O. Accordingly, TPO results and SEM images on the post-OCM LSNF cells indicate that the co-feeding of H_2O during OCM effectively prevented carbon from being deposited on the surface of the LSNF cell resulting in the polarization resistance being reduced. It has been reported that a few percent of H_2O significantly improved the catalytic performance on methane dehydrogenation reaction.[38] Higher concentration of H_2O may hinder the diffusion of CH_4 near the surface leading to the increase of the R_{LF}.

A further investigation was conducted using in-situ DRIFTS under CH_4 at 450 °C as shown in Figure 12. Two strong peaks located at 3015 cm^{-1} and 1300 cm^{-1} are attributed to the asymmetric C–H stretch (*v3*) and bending of CH_4, respectively.[39] The DRIFTS spectrum on LSNF catalysts shows two additional small peaks at 2360 cm^{-1} and 2330 cm^{-1} associated with molecularly adsorbed CO_2.[32a,34] These peaks are due to deep oxidation of CH_4 on the LSNF surface. In contrast, the IR bands corresponding to C_2H_6 were found at 1460 cm^{-1} and 860 cm^{-1} only on the Red-LSNF under CH_4, without co-feeding of H_2O.[40] This result indicates that the Red-LSNF catalyst is selective toward C_2H_6 formation and effectively inhibits the deep oxidation of CH_4 to CO_2. Under CH_4 flow with 3% H_2O in Figure 12(c), the DRIFTS spectrum shows that small molecular CO_2 peaks and the OH bending vibration of H_2O in 1800–1400 cm^{-1}.[41] The broad band of H_2O located between 3100 cm^{-1} and 3500 cm^{-1} was not observed because the operating temperature of 450 °C is too high to form the stretching modes of hydrogen-bonded OH.[42] The IR band of C_2H_6 was also not detected suggesting that the H_2O molecules may prevent adsorption of C_2H_6 or promote the desorption of C_2H_6 by saturating the surface of the Red-LSNF. Since C_2H_6 is more susceptible to the deep oxidation to CO_2 than CH_4, the enhanced desorption of C_2H_6 is likely to decrease the deep oxidation to CO_2. As such, co-feeding with H_2O could be an effective method of increasing selectivity and production rate of C_{2+} hydrocarbons for the electrocatalytic OCM.

Conclusion

The oxidative coupling of methane (OCM) selective towards C_{2+} hydrocarbons was accomplished electrocatalytically by making use of solid oxide cells that provide easy control of oxygen supply through solid oxide electrolytes. LSNF perovskites effectively performed for the electrocatalytic OCM as an anode and the improvement of their surface characteristics induced by the reduction and the resultant exsolution of NiFe nanoparticles were evaluated by various techniques. XRD and ETEM analysis proved that bimetallic NiFe nanoparticles were evenly exsolved on the surface of LSNF under a reducing environment at elevated temperatures. An observation of the firm attachment of exsolved NiFe nanoparticles to the surface of the perovskite parent with a dynamic lateral movement was made through a real time video using ETEM. An analysis of XPS revealed the reduction treatment of LSNF resulted in a decrease in the surface elemental oxidation state of iron atoms, partially down to zerovalent species, and an increase in the surface adsorbed species on O 1s and Sr 3d spectra, indicative of oxygen vacancy formation. The in-situ TPD-DRIFTS with CO_2 as a probe molecule indicates an increase in LSNF basicity, which is one of the key characteristics of activating weakly acidic CH_4. Compared with the LSNF, the production rate of C_{2+} hydrocarbons on the Red-LSNF improved 35.3% for the electrocatalytic OCM. The OCM reaction on the Red-LSNF was electrocatalytically activated to produce 11 times more C_{2+} hydrocarbons. Additionally, co-feeding of H_2O enhanced the selective conversion of CH_4, resulting in a 56% increase in the production rate of C_{2+} hydrocarbons. Analysis of impedance spectra and in-situ DRIFTS under CH_4 with H_2O suggested that the improvement of the electrocatalytic OCM results is likely due to the saturated coverage of H_2O molecules on the Red-LSNF surface.

Experimental

Preparation of catalysts

The citric acid-ethylenediaminetetraacetic acid (EDTA) complexation method was employed to prepare $La_{0.7}Sr_{0.2}Ni_{0.2}Fe_{0.8}O_3$ (LSNF), as previously reported.[41a] Stoichiometric amounts of metal-nitrate salts were dissolved in 100 ml of deionized water. A 1:1 molar ratio of EDTA to the total metal ions was added to the solution at room temperature. At 60 °C, ammonium hydroxide was added to the solution to stabilize the pH at 6. After adding ethylene glycol and citric acid, the solution was heated to 90 °C, maintaining a pH of 6. Afterward, the gel formed was dried at 150 °C. Crystalline LSNF was obtained by calcining dried black powder for 2 h at 1000 °C. The calcined LSNF powders were reduced at 800 °C under 5% H_2/N_2 to produce Red-LSNF samples.

Evaluation of electrochemical performance

A button cell was fabricated using a screen-printing technique on a commercial Yttria-stabilized zirconia (YSZ) electrolyte (25 mm in diameter, 125 μm in thickness; Nextech Materials). An interlayer of gadolinium-doped ceria (GDC; Nextech Materials) was screen-printed on the anode side and sintered for 2 h at 1400 °C in air. The LSNF was mixed with GDC at 40 wt% and the mixture was screen-printed on the top of the GDC buffer layer to cover an area of 0.72 cm^2, then sintered under vacuum at 1200 °C. A 50 wt% $(La_{0.80}Sr_{0.20})_{0.95}MnO_3$-50 wt% $(Y_2O_3)_{0.08}(ZrO_2)_{0.92}$ (LSM-YSZ; Nextech Materials) mixture was screen-printed and sintered at 1200 °C under air for 2 h. A gold paste was used to attach the gold wire and gold grid to the electrodes as current collectors. The experimental setup for OCM is illustrated in Figure S7. During electrocatalytic runs, 10 ccm of 99.99% CH_4 was flowed into the anode side and the operating temperature was at 800 °C. The cathode side was open to atmosphere. The electrochemical impedance spectrum (EIS) was collected with frequencies ranging from 1 MHz to 10 mHz using a potentiostat (BioLogic). Distribution of relaxation time was analyzed using a DRTtools.[35] The gas products were quantified using a pulse discharge helium ionization detector (PDHID) and a flame ionization detector (FID) in an on-line gas chromatograph (Shimadzu 2014). The methane conversion was calculated based on the methane concentration difference between the feed and the effluent (Eq. 5),

$$X_{CH_4} = \frac{y^{in}_{CH_4} - y^{out}_{CH_4}}{y^{in}_{CH_4}} \times 100\,\% \quad (5)$$

where $y^{in}_{CH_4}$ and $y^{out}_{CH_4}$ are the methane mole fractions in the feed and the effluent stream, respectively. The selectivity for the hydrocarbon species *j* was calculated as (Eq. 6):

$$S_j = \frac{n_j y_j}{\sum n_i y_i} \times 100\,\% \quad (6)$$

where *n* is the number of carbon atoms in the molecule of the hydrocarbon product.

Characterization

Bruker D8 Lead X-ray powder diffractometer equipped with Cu Kα X-ray source was used to acquire the X-ray diffraction patterns. The voltage and current in the generator were 40 kV and 40 mA, respectively. The 2θ scan range was 20°–60° and the step size was 0.014° per 0.5 s. An open crystallographic database (COD) was used to identify phases.[43] The Rietveld refinement method was used to determine Miller indices and weight fractions for each phase using General Structure Analysis System-2 (GSAS-2).[44]

A MKS Cirrus mass spectrometer was used to analyze the effluent produced by the temperature-programmed reduction (TPR) of 30 sccm of 5% H_2/N_2. Catalyst powders were filled into the reactor and the temperature was ramped up from room temperature to 1000 °C with a ramp rate of 10 °C min^{-1}. Temperature-programmed oxidation (TPO) was conducted for the post-OCM LSNF cells under 30 sccm of 10% O_2/He with a ramp rate of 10 °C min^{-1}.

Environmental transmission electron microscopy (ETEM) characterization was conducted with a FEI Titan ETEM G2 80–300 kV instrument equipped with an objective Cs aberration corrector. Mass flow controllers and mass spectrometers monitored the effluent under various temperatures and 1 mbar H_2 atmospheres for the ETEM study. Using a mass spectrometer (Pfeiffer), the concentration of hydrogen was continually measured. Inverse Fast Fourier Transform (IFFT) was conducted using Image J program.[45] The scanning transmission electron microscope (STEM) was used for an investigation of Red-LSNF using a TECNAI F20 TEM operating at 200 kV equipped with an energy dispersive X-ray spectroscopy (EDS).

SEM backscattered electron images were taken in an FEI Apreo instrument at an accelerating voltage of 20 kV and 0.2 nA beam current.

Raman spectra of the samples were collected in a Horiba HR800 Raman microscope equipped with 514.5 nm wavelength argon ion laser as the radiation source.

X-ray photoelectron Spectroscopy (XPS) was employed to investigate the surface elemental oxidation state and composition using a Kratos Axis Ultra XPS instrument. It is equipped with a monochromated Al Kα X-ray source (1254 eV, 12 kV, 10 mA) and a charge neutralizer at 2.05 A of element current, 1.3 V of filament bias, and 3.6 V of charge balance. Calibration for each scan was based on the C 1s standard peak at 284.5 eV.

Thermoelectron Nicolet 6700 FTIR equipped with an MCT detector was used to collect temperature-programmed desorption (TPD) - diffuse reflectance infrared Fourier transform spectroscopy (DRIFTS) data. A 1:20 ratio of catalyst-to-potassium bromide (KBr) was used for dilution of powder samples. Helium pretreatment of the samples at 450 °C was performed to desorb any species adsorbed prior to the experiment. DRIFTS spectra were collected at various temperatures under helium after samples were exposed to CO_2 at 50 °C for in-situ TPD-DRIFTS of CO_2. For in-situ DRIFTS under CH_4, the DRIFTS spectra of the pretreated samples were acquired under 30 ccm of 10% CH_4/He at 450 °C with or without 3% H_2O.

Acknowledgements

We would like to gratefully acknowledge the financial support provided for this work by the U.S. Department of Energy, Office of Science, Office of Basic Energy Sciences under the Award Number DE-FG02-07ER15896 and the U.S. National Science Foundation, under the award number 1932638. STEM images were acquired at the Center for Electron Microscopy and Analysis (CEMAS) at the Ohio State University.

Conflict of Interest

The authors declare that they have no known competing financial interests or personal relationships that could have appeared to influence the work reported in this paper.

Data Availability Statement

The data that support the findings of this study are available from the corresponding author upon reasonable request.

Keywords: C–C coupling · electrocatalysis · exsolution · perovskite phases · solid oxide electrocatalytic cell

[1] E. McFarland, *Science* **2012**, *338*, 340–342.
[2] a) C. Zhu, S. Hou, X. Hu, J. Lu, F. Chen, K. Xie, *Nat. Commun.* **2019**, *10*, 1173; b) M. Ma, B. J. Jin, P. Li, M. S. Jung, J. I. Kim, Y. Cho, S. Kim, J. H. Moon, J. H. Park, *Adv. Sci.* **2017**, *4*, 1700379; c) C. Oh, J. Kim, Y. J. Hwang, M. Ma, J. H. Park, *Appl. Catal. B* **2021**, *283*; d) M. S. A. Sher Shah, C. Oh, H. Park, Y. J. Hwang, M. Ma, J. H. Park, *Adv. Sci.* **2020**, *7*, 2001946; e) S. Kodama, R. Kikuchi, N. Fujiwara, S. Tada, Y. Kobayashi, S. T. Oyama, *ECS Trans.* **2019**, *91*, 2697–2705; f) J. Lu, C. Zhu, C. Pan, W. Lin, J. P. Lemmon, F. Chen, C. Li, K. Xie, *Sci. Adv.* **2018**, *4*, eaar5100.
[3] C. A. Ortiz-Bravo, C. A. Chagas, F. S. Toniolo, *J. Nat. Gas Sci. Eng.* **2021**, *96*, 104254.
[4] K. Liu, J. Zhao, D. Zhu, F. Meng, F. Kong, Y. Tang, *Catal. Commun.* **2017**, *96*, 23–27.
[5] Z. Stansch, L. Mleczko, M. Baerns, *Ind. Eng. Chem. Res.* **1997**, *36*, 2568–2579.
[6] a) V. Kyriakou, I. Garagounis, M. Stoukides, *Int. J. Hydrogen Energy* **2014**, *39*, 675–683; b) I. M. Petrushina, V. A. Bandur, N. J. Bjerrum, F. Cappeln, L. Qingfeng, *J. Electrochem. Soc.* **2002**, *149*, D143–D147; c) S. A. Venâncio, P. E. V. de Miranda, *Int. J. Hydrogen Energy* **2017**, *42*, 13927–13938.
[7] a) Y. S. Su, J. Y. Ying, W. H. Green Jr, *J. Catal.* **2003**, *218*, 321–333; b) B. L. Farrell, V. O. Igenegbai, S. Linic, *ACS Catal.* **2016**, *6*, 4340–4346.
[8] T. Karasuda, K. Nagaoka, K.-I. Aika, *Stud. Surf. Sci. Catal.* **1998**, *119*, 283–288.
[9] T. Kazuhiro, I. Enrique, *J. Phys. Chem. C* **2009**, *113*, 10131–10145.
[10] V. Lomonosov, Y. Gordienko, M. Sinev, *Top. Catal.* **2013**, *56*, 1858–1866.
[11] S. Gunduz, D. Dogu, D. J. Deka, K. E. Meyer, A. Fuller, A. C. Co, U. S. Ozkan, *Catal. Today* **2019**, *323*, 3–13.
[12] a) B. D. Madsen, W. Kobsiriphat, Y. Wang, L. D. Marks, S. A. Barnett, *J. Power Sources* **2007**, *166*, 64–67; b) W. Kobsiriphat, B. D. Madsen, Y. Wang, M. Shah, L. D. Marks, S. A. Barnett, *J. Electrochem. Soc.* **2010**, *157*, B279–B284.
[13] L. Sangaletti, L. E. Depero, B. Allieri, P. Nunziante, E. Traversa, *J. Eur. Ceram. Soc.* **2001**, *21*, 719–726.
[14] T. J. B. Holland, S. A. T. Redfern, *Mineral. Mag.* **1997**, *61*, 65–77.
[15] E. H. Yang, Y. S. Noh, S. S. Lim, B. S. Ahn, D. J. Moon, *J. Nanosci. Nanotechnol.* **2016**, *16*, 1938–1941.
[16] S. Liu, Q. Liu, J.-L. Luo, *ACS Catal.* **2016**, *6*, 6219–6228.
[17] F. Gonzalez Garcia, C. S. Riccardi, A. Z. Simões, *J. Alloys Compd.* **2010**, *501*, 25–29.
[18] S. Upasen, P. Batocchi, F. Mauvy, A. Slodczyk, P. Colomban, *J. Alloys Compd.* **2015**, *622*, 1074–1085.
[19] G. Nirala, D. Yadav, S. Upadhyay, *J. Adv. Ceram.* **2020**, *9*, 129–148.
[20] Y. R. Jo, B. Koo, M. J. Seo, J. K. Kim, S. Lee, K. Kim, J. W. Han, W. Jung, B. J. Kim, *J. Am. Chem. Soc.* **2019**, *141*, 6690–6697.
[21] Y. Gao, D. Chen, M. Saccoccio, Z. Lu, F. Ciucci, *Nano Energy* **2016**, *27*, 499–508.

[22] a) D. Neagu, G. Tsekouras, D. N. Miller, H. Menard, J. T. Irvine, *Nat. Chem.* **2013**, *5*, 916–923; b) O. Kwon, S. Sengodan, K. Kim, G. Kim, H. Y. Jeong, J. Shin, Y. W. Ju, J. W. Han, G. Kim, *Nat. Commun.* **2017**, *8*, 15967; c) T. Zhu, H. Troiani, L. V. Mogni, M. Santaya, M. Han, S. A. Barnett, *J. Power Sources* **2019**, *439*.
[23] a) Y. Wang, T. Liu, M. Li, C. Xia, B. Zhou, F. Chen, *J. Mater. Chem. A* **2016**, *4*, 14163–14169; b) Z. Du, H. Zhao, S. Yi, Q. Xia, Y. Gong, Y. Zhang, X. Cheng, Y. Li, L. Gu, K. Swierczek, *ACS Nano* **2016**, *10*, 8660–8669; c) T. Zhang, Y. Zhao, X. Zhang, H. Zhang, N. Yu, T. Liu, Y. Wang, *ACS Sustainable Chem. Eng.* **2019**, *7*, 17834–17844.
[24] C. Yang, Z. Yang, C. Jin, G. Xiao, F. Chen, M. Han, *Adv. Mater.* **2012**, *24*, 1439–1443.
[25] M. Descostes, F. Mercier, N. Thromat, C. Beaucaire, M. Gautier-Soyer, *Appl. Surf. Sci.* **2000**, *165*, 288–302.
[26] a) W. Y. Hernández, M. N. Tsampas, C. Zhao, A. Boreave, F. Bosselet, P. Vernoux, *Catal. Today* **2015**, *258*, 525–534; b) Z. Zhao, H. Dai, J. Deng, Y. Du, Y. Liu, L. Zhang, *Microporous Mesoporous Mater.* **2012**, *163*, 131–139.
[27] D. J. Deka, S. Gunduz, T. Fitzgerald, J. T. Miller, A. C. Co, U. S. Ozkan, *Appl. Catal. B* **2019**, *248*, 487–503.
[28] a) D. Kim, J. W. Park, M. S. Chae, I. Jeong, J. H. Park, K. J. Kim, J. J. Lee, C. Jung, C.-W. Lee, S.-T. Hong, K. T. Lee, *J. Mater. Chem. A* **2021**, *9*, 5507–5521; b) A. Machocki, T. Ioannides, B. Stasinska, W. Gac, G. Avgouropoulos, D. Delimaris, W. Grzegorczyk, S. Pasieczna, *J. Catal.* **2004**, *227*, 282–296.
[29] a) K. Rida, A. Benabbas, F. Bouremmad, M. A. Peña, A. Martínez-Arias, *Catal. Commun.* **2006**, *7*, 963–968; b) E. J. Crumlin, E. Mutoro, Z. Liu, M. E. Grass, M. D. Biegalski, Y.-L. Lee, D. Morgan, H. M. Christen, H. Bluhm, Y. Shao-Horn, *Energy Environ. Sci.* **2012**, *5*, 6081–6088.
[30] A. K. Opitz, A. Nenning, C. Rameshan, M. Kubicek, T. Gotsch, R. Blume, M. Havecker, A. Knop-Gericke, G. Rupprechter, B. Klotzer, J. Fleig, *ACS Appl. Mater. Interfaces* **2017**, *9*, 35847–35860.
[31] a) L. Ye, C. Pan, M. Zhang, C. Li, F. Chen, L. Gan, K. Xie, *ACS Appl. Mater. Interfaces* **2017**, *9*, 25350–25357; b) A. K. Opitz, C. Rameshan, M. Kubicek, G. M. Rupp, A. Nenning, T. Gotsch, R. Blume, M. Havecker, A. Knop-Gericke, G. Rupprechter, B. Klotzer, J. Fleig, *Top. Catal.* **2018**, *61*, 2129–2141.
[32] a) J. C. Lavalley, *Catal. Today* **1996**, *27*, 377–401; b) D. Dogu, S. Gunduz, K. E. Meyer, D. J. Deka, A. C. Co, U. S. Ozkan, *Catal. Lett.* **2019**, *149*, 1743–1752.
[33] L. Ye, M. Zhang, P. Huang, G. Guo, M. Hong, C. Li, J. T. Irvine, K. Xie, *Nat. Commun.* **2017**, *8*, 14785.
[34] D. J. Deka, J. Kim, S. Gunduz, M. Aouine, J.-M. M. Millet, A. C. Co, U. S. Ozkan, *Appl. Catal. B* **2021**, *286*, 119917.
[35] T. H. Wan, M. Saccoccio, C. Chen, F. Ciucci, *Electrochim. Acta* **2015**, *184*, 483–499.
[36] E. Hernández, F. Baiutti, A. Morata, M. Torrell, A. Tarancón, *J. Mater. Chem. A* **2018**, *6*, 9699–9707.
[37] a) V. Kharton, E. Tsipis, I. Marozau, A. Viskup, J. Frade, J. Irvine, *Solid State Ionics* **2007**, *178*, 101–113; b) S. Yu, D. Yoon, Y. Lee, H. Yoon, H. Han, N. Kim, C. J. Kim, K. Ihm, T. S. Oh, J. Son, *Nano Lett.* **2020**, *20*, 3538–3544.
[38] a) S. Liu, *J. Catal.* **2003**, *220*, 57–65; b) T. Zhu, Z. Yang, M. Han, *Fuel* **2015**, *161*, 168–173.
[39] a) G. Molpeceres, M. A. Satorre, J. Ortigoso, C. Millán, R. Escribano, B. Maté, *ApJ* **2016**, *825*, 156; b) J. Kim, Y. J. Kim, M. Ferree, S. Gunduz, A. C. Co, M. Kim, U. S. Ozkan, *Appl. Catal. B* **2023**, *321*, 122026.
[40] B. Shri Prakash, S. Senthil Kumar, S. T. Aruna, *Bull. Mater. Sci.* **2017**, *40*, 441–452.
[41] a) J. Kim, M. Ferree, S. Gunduz, J.-M. M. Millet, M. Aouine, A. C. Co, U. S. Ozkan, *J. Mater. Chem. A* **2022**, *10*, 2483–2495; b) Y.-C. Liu, C.-H. Yeh, Y.-F. Lo, S. Nachimuthu, S. D. Lin, J.-C. Jiang, *J. Catal.* **2020**, *385*, 265–273.
[42] A. Litke, Y. Su, I. Tranca, T. Weber, E. J. M. Hensen, J. P. Hofmann, *J. Phys. Chem. C* **2017**, *121*, 7514–7524.
[43] A. Vaitkus, A. Merkys, S. Grazulis, *J. Appl. Crystallogr.* **2021**, *54*, 661–672.
[44] B. H. Toby, R. B. Von Dreele, *J. Appl. Crystallogr.* **2013**, *46*, 544–549.
[45] C. A. Schneider, W. S. Rasband, K. W. Eliceiri, *Nat. Methods* **2012**, *9*, 671–675.

Manuscript received: November 1, 2022
Revised manuscript received: February 27, 2023
Accepted manuscript online: February 28, 2023
Version of record online: March 20, 2023